ADVANCED ENERGY MATERIALS
www.advenergymat.de

Ostwald Ripening of Ag_2Te Precipitates in Thermoelectric PbTe: Effects of Crystallography, Dislocations, and Interatomic Bonding

Yuan Yu, Ariel Sheskin, Zhenyu Wang,* Aleksandra Uzhansky, Yuriy Natanzon, Muhamed Dawod, Lamya Abdellaoui, Torsten Schwarz, Christina Scheu, Matthias Wuttig, Oana Cojocaru-Mirédin, Yaron Amouyal,* and Siyuan Zhang**

Nanostructuring is important for designing thermoelectrics. Yet, nanoprecipitates are thermodynamically unstable and coarsen through Ostwald ripening. Here, the Ostwald ripening of Ag_2Te in PbTe and its resulting impact on thermoelectric performance is investigated. Numerous Guinier-Preston zones and platelet Ag_2Te precipitates in the sample quenched from a single-phase region is observed. Upon annealing, these platelet precipitates grow into big lath-shaped second phases by consuming small Ag-rich clusters. The crystallographic orientation relationships between Ag_2Te and PbTe are unraveled by scanning transmission electron microscopy and modeled by first-principles calculations. The interfaces with low lattice mismatch determine the morphology of Ag_2Te in PbTe. Atom probe tomography reveals different chemical bonding mechanisms for PbTe and Ag_2Te, which are metavalent and iono-covalent, respectively. This leads to an acoustic phonon mismatch at the precipitate-matrix interface. Yet, the electrons are also scattered by these interfaces, resulting in poor electrical properties in the as-quenched sample. In contrast, the annealed sample contains abundant Ag-decorated dislocations by activating the Bardeen-Herring source. These dislocations strongly scatter phonons while maintaining a good electron transmission, contributing to a higher thermoelectric performance. This work demonstrates the complex role of microstructure morphologies, compositions, and bonding mechanisms in thermoelectric response, providing insights into structural design for thermoelectrics.

1. Introduction

Thermoelectric (TE) materials can directly convert heat into electricity and vice versa without byproducts, providing a sustainable and clean energy solution.[1–7] The energy conversion efficiency is determined by the figure-of-merit, $zT = S^2\sigma T/\kappa_{tot}$, where S is the Seebeck coefficient, σ the electrical conductivity, κ_{tot} the total thermal conductivity contributed from the charge transport, κ_{ele}, and lattice vibrations, κ_{lat}, and T is the absolute temperature. These parameters involve delicate interweaving between electrons and phonons, making the improvement of zT challenging.[2–5] The most prevalent strategies for enhancing zT rely on judiciously introducing various structural defects ranging from atomistic point defects to microscale precipitates.[3–5,8,18]

Aliovalent doping has been routinely adopted to donate or accept electrons since the TE performance optimizes within a narrow carrier concentration range, typically between 10^{19} and 10^{21} cm^{-3}.[4,19–21] A homogeneous

Y. Yu, M. Wuttig, O. Cojocaru-Mirédin
Institute of Physics (IA)
RWTH Aachen University
Sommerfeldstraße 14, 52074 Aachen, Germany
E-mail: yu@physik.rwth-aachen.de

The ORCID identification number(s) for the author(s) of this article can be found under https://doi.org/10.1002/aenm.202304442

DOI: 10.1002/aenm.202304442

A. Sheskin, A. Uzhansky, Y. Natanzon, M. Dawod, Y. Amouyal
Department of Materials Science and Engineering
Technion – Israel Institute of Technology
Technion City
Haifa 32000, Israel
E-mail: amouyal@technion.ac.il

Z. Wang, L. Abdellaoui, T. Schwarz, C. Scheu, S. Zhang
Max-Planck Institut für Eisenforschung GmbH
40237 Düsseldorf, Germany
E-mail: zwang@mpie.de; siyuan.zhang@mpie.de

M. Wuttig
Green IT (PGI 10)
Forschungszentrum Jülich GmbH
52428 Jülich, Germany

O. Cojocaru-Mirédin
Department of Sustainable Systems Engineering (INATECH)
Albert-Ludwigs-Universität Freiburg
79110 Freiburg, Germany

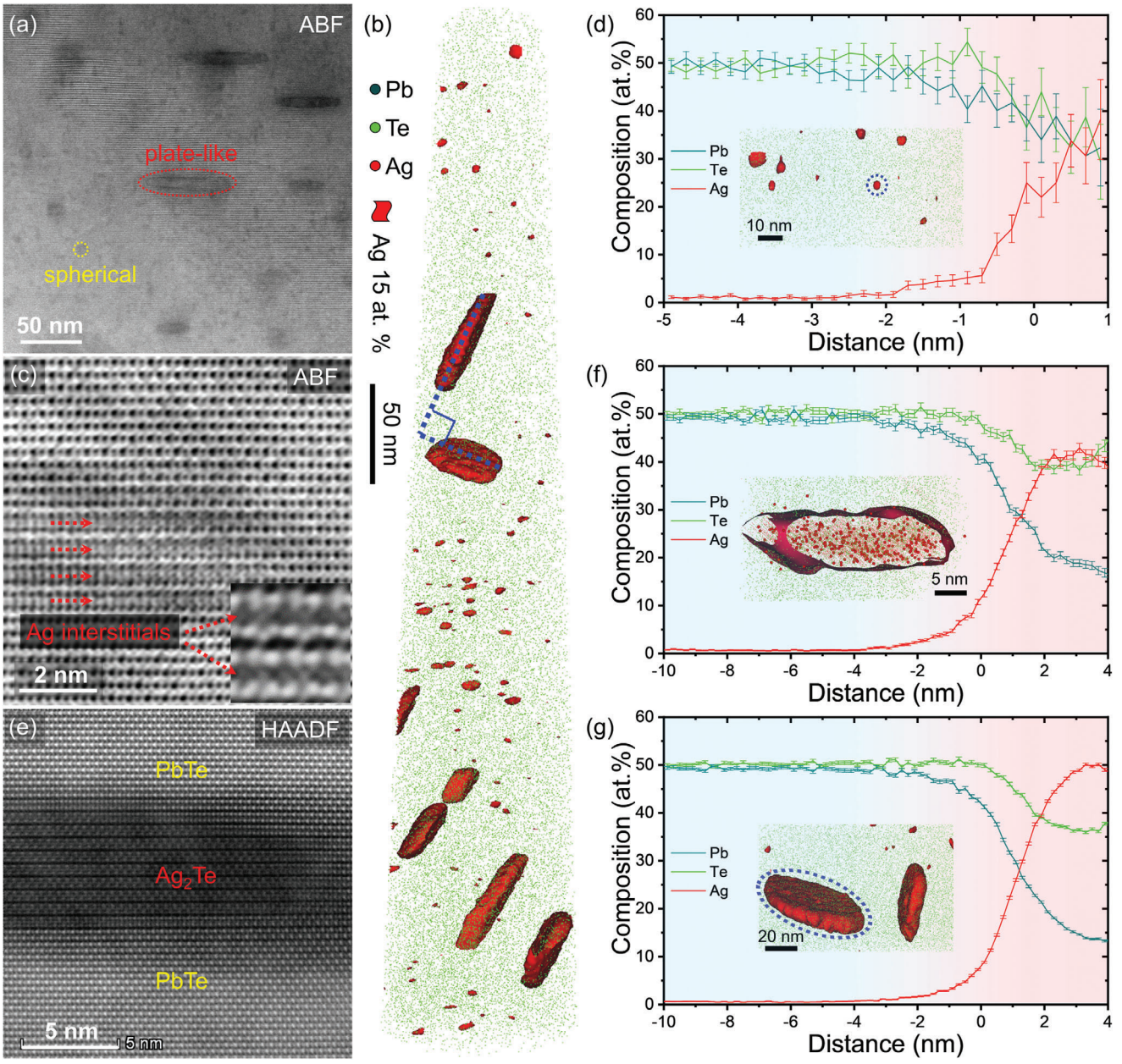

Figure 1. Scanning transmission electron microscopy (STEM) and atom probe tomography (APT) characterization for the as-quenched sample. a) Annular bright field (ABF) image showing various defects with different morphologies and sizes; one big plate-like and one small spherical defect are indicated by the red and yellow dotted line, respectively, for close-up investigations; b) 3D reconstruction showing the distribution of Te (green dots) and Ag-rich defects (15 at.% Ag iso-composition surface). For clarity, the point cloud of Pb is omitted. c) ABF image of the small spherical defect with interstitial Ag atoms indicated by red arrows; inset is a magnified high-angle annular dark field (HAADF) image showing the interstitial atoms. d) Proximity histogram showing the composition profile across the iso-surface of the small defect circled by blue dotted lines in the inset. e) HAADF image of the area containing the large plate-like defect. f) Proximity histogram of a medium-size (≈20 nm in diameter) plate-like defect with its shape given in the inset. g) Proximity histogram of a large (≈55 nm in diameter) plate-like defect with its shape given in the inset.

distribution of dopants is favored to enable high doping efficiency and in most cases is even the default scenario. However, some dopants cannot completely dissolve into the matrix due to their low thermodynamic solubility limit, resulting in the formation of precipitates and other solute-rich defects.[4,5,8,22–24] Incorporating nanostructures into thermoelectrics has been intensively studied in the last decades since it was believed to reduce thermal conductivity while barely sacrificing charge carrier mobility.[25–28] Yet, this ideal presumption proved to be unjustified in many cases because the lattice defects scatter both phonons and electrons, giving rise to a compromise between the lattice thermal conductivity and carrier mobility.[29–31] Moreover, not all structural defects are effective in scattering phonons, but only those with large mass contrast and significant strain fields

Table 1. The orientation relationship (OR) between Ag_2Te ($P2_1/c$) precipitates and the PbTe matrix ($Fm\bar{3}m$) fulfills all three conditions OR-a, OR-b, and OR-c, with their corresponding lattice plane spacings and mismatches listed in separate columns.

Orientation relationships (OR)	Ag_2Te	PbTe	Lattice mismatch
OR-a $[201]_{Ag_2Te} \parallel [001]_{PbTe}$	(200) 3.38 Å	(002) 3.23 Å	4.6%
OR-b $[010]_{Ag_2Te} \parallel [1\bar{1}0]_{PbTe}$	(020) 2.23 Å	$(2\bar{2}0)$ 2.28 Å	−2.2%
OR-c $[001]_{Ag_2Te} \parallel [110]_{PbTe}$	$(\bar{2}04)$ 2.24 Å	(220) 2.28 Å	−1.7%

between the defects and the matrix.[32,33] It is recently found that the nature of chemical bonding is also important for interfacial phonon scattering.[34,35] More importantly, these nanoscale lattice defects might be thermally unstable and thus impact the dynamic TE properties and service stability.[36–38] Determination of the existing forms of defects including their morphology, number density, chemical composition, and chemical bonding mechanism, as well as how they evolve with annealing, can improve our understanding of defect engineering for designing TE materials.

Lattice defects have been widely implemented in Pb chalcogenides to obtain improved TE properties such as nanoprecipitates in PbTe[39–42] and dislocations in PbX (X = Se, Te).[9–13,20,21,43–47] Yet, the structural evolution of defects has been investigated in much fewer studies.[38,48–50] Since the phase diagram of the PbTe-Ag_2Te system has been well described,[51,52] we design microstructures in PbTe-Ag_2Te alloys to study the structural evolution with annealing and its concomitant impact on the TE properties. In particular, Ag_2Te precipitates were proven to be effective in scattering phonons and were thus subject to intensive research.[53–55] Previous works by Lensch-Falk et al.,[49] Grossfeld et al.,[36] and Sheskin et al.[37] have provided insights into the precipitation and coarsening of Ag_2Te in PbTe, but the nucleation and growth mechanism of precipitates, the detailed interfacial atomic structures and compositions, the chemical bonding mechanisms, and their impact on the TE properties were not fully understood.

In this work, we have controlled the nucleation and growth of precipitates in a $(PbTe)_{0.97}(Ag_2Te)_{0.03}$ alloy according to the PbTe-Ag_2Te phase diagram using water quenching and thermal annealing.[51,52] The microstructure evolution was investigated by scanning transmission electron microscopy (STEM) and atom probe tomography (APT).[56] The microstructural features such as the precipitate size, number density, composition, and chemical bonding mechanism were correlated with the TE properties. A high number density of iono-covalently bonded Ag_2Te precipitates and Guinier-Preston (GP) zones was found in the metavalently bonded PbTe matrix in the as-quenched sample. The large precipitates coarsen by consuming small precipitates through the Ostwald ripening mechanism upon annealing. High-density dislocations were also observed in the annealed sample. Even though these nanoprecipitates can strongly scatter phonons, the electrical conductivity is seriously degraded as well. In contrast, dislocations are more favorable to thermoelectrics because they can scatter phonons while maintaining electron transmission. This work thus provides an in-depth understanding of the relationship between microstructure, composition, chemical bonding, and TE properties of PbTe-Ag_2Te-based TE materials. These relationships between structures and properties can, in turn, guide the design of other thermoelectrics.

2. Results and Discussion

2.1. Microstructure Investigations

Figure 1a reveals the annular bright field (ABF)-STEM image that shows the diffraction contrast of precipitates with various morphologies and sizes in the as-quenched sample. A large plate-like and a small spherical precipitate are highlighted by the red and yellow dotted circles, respectively. 3D morphologies of these precipitates are delineated by the iso-composition surfaces containing more than 15 at.% Ag in APT reconstruction (Figure 1b). The small precipitates are spherical with diameters of 1–5 nm and a number density of $\approx 7.5 \times 10^{24}$ m^{-3}. The larger plate-like precipitates have an average radius of 20–30 nm and a number density of $\approx 1.9 \times 10^{21}$ m^{-3}. The STEM micrograph shows interstitial atoms within the spherical precipitates, as indicated by the red arrows in Figure 1c. An APT composition proximity histogram reveals that the small spherical precipitate has an Ag-rich core with a maximum concentration of ≈30 at.%, while Pb and Te are 1:1 in composition (Figure 1d). This confirms the STEM observation that Ag atoms mainly occupy the interstitial positions within such a small spherical region, which is also consistent with the low defect formation energy of Ag interstitials in PbTe obtained by density functional theory (DFT) calculations.[21] Note that we cannot exclude the existence of Ag atoms substituting Pb. The small clusters are Ag-enriched, metastable regions in PbTe formed as GP zones,[57] from which bigger, stable Ag_2Te plate-like precipitates nucleate.

A plate-like precipitate is atomically resolved in Figure 1e, and identified to be monoclinic Ag_2Te (space group $P2_1/c$) which is known to be stable below 140 °C.[49] The Ag_2Te precipitate fulfills three orientation relationships (OR) with the PbTe matrix, listed as RO-a, OR-b, and OR-c in **Table 1**. It is noteworthy that for monoclinic Ag_2Te, the normal direction of (200) planes is parallel to [201], whereas the *c*-axis direction [001] is parallel to the normal of $(\bar{2}04)$ planes. The transitions from the triple-layer motif of Ag_2Te (parallel to $(200)_{Ag_2Te}$) to the alternating Pb-Te motif are observed along the direction normal to $(002)_{PbTe}$, corresponding to OR-a. The zone axes of Ag_2Te and PbTe fulfill the OR-c. More details of the atomic structure of the interface can be found in Figure S1 (Supporting Information). The overlapping atomic models for PbTe and Ag_2Te demonstrate that the middle Ag layer in the triple-layer motif of Ag_2Te corresponds to the interstitial positions of PbTe. Other Ag atoms correspond to the cationic Pb positions while the anionic Te positions extend from PbTe to Ag_2Te. We have also observed the relationship between Ag_2Te and PbTe along the zone axes described in OR-b, as shown in Figure S2 (Supporting Information) and summarized in Table 1. The large lattice mismatch between $(200)Ag_2Te$ and $(002)_{PbTe}$ (OR-a) determines the habit plane for Ag_2Te growth. Within a given PbTe grain, all habit planes of the precipitates $(200)Ag_2Te$ are parallel to $(002)_{PbTe}$, which are either parallel or perpendicular to each other. As a result, Ag_2Te precipitates captured in the APT (Figure 1b) results show such orientation relationships. The composition of the plate-like defect is close to Ag_2Te with a certain amount of Pb solute atoms (Figure 1f). The

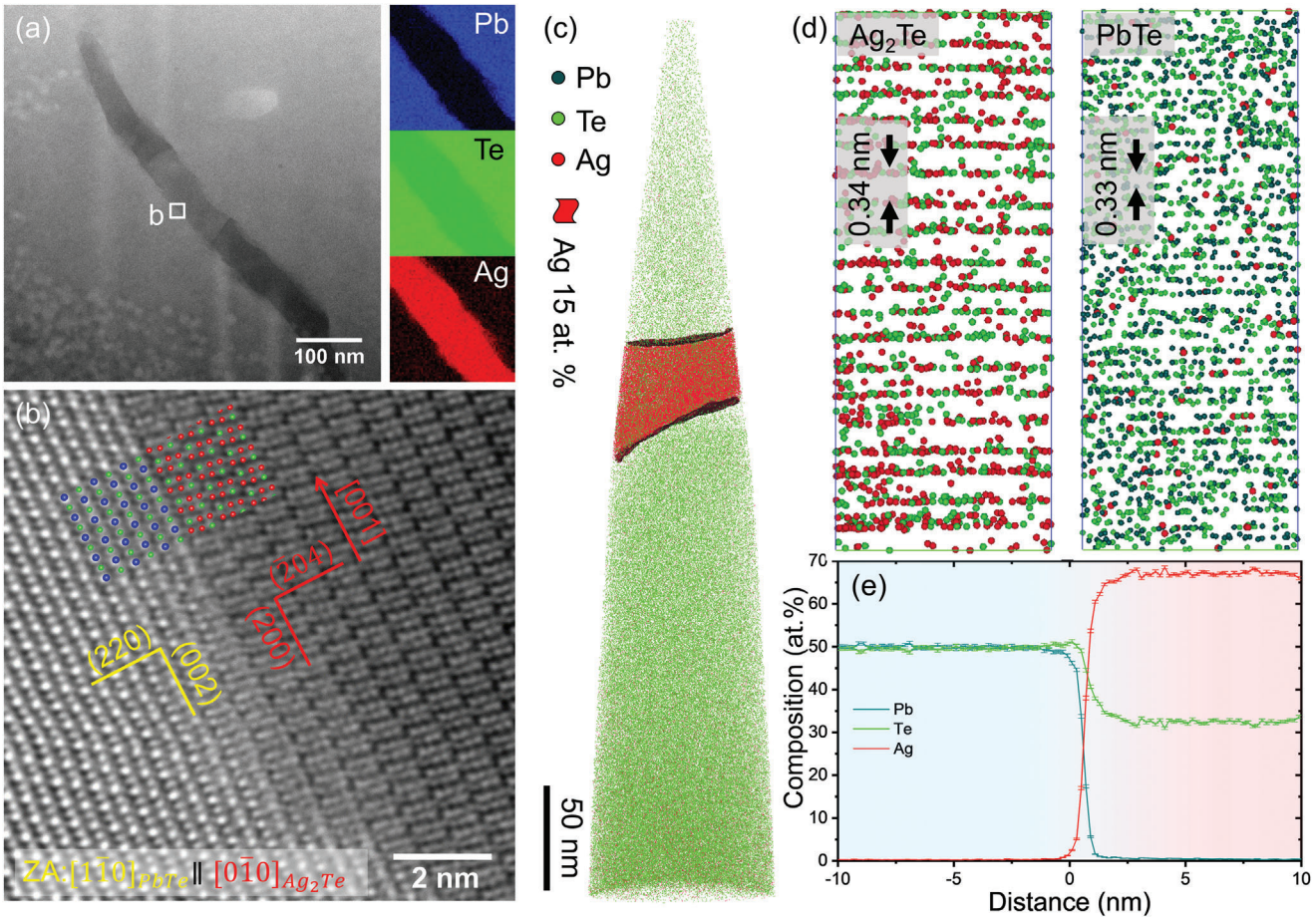

Figure 2. STEM and APT results of the 48 h-annealed sample. a) HAADF image and energy dispersive X-ray spectroscopy (EDS) mapping showing a large plate-like Ag_2Te precipitate; b) phase boundary between PbTe matrix and Ag_2Te precipitate with parallel planes indicated. c) APT reconstruction showing the distribution of Te and Ag, Pb is omitted for clarity; phase boundaries are highlighted by 15 at. % Ag iso-composition surface. d) Lattice planes reconstructed in the vicinity of poles showing the (200) plane of Ag_2Te and (002) plane of PbTe. e) Proximity histogram presenting the composition profile crossing from PbTe matrix to Ag_2Te precipitate.

larger the size of the precipitate, the more Ag and fewer Pb atoms are within the precipitate (Figure 1f,g). This demonstrates that the growth of Ag_2Te is accompanied by repelling Pb out of the Ag_2Te phase and absorbing Ag from the PbTe matrix, indicating the essence of Ag-diffusion in the PbTe matrix.[58] We observed fewer numbers of Ag-rich clusters around the big Ag_2Te precipitates in Figure 1b, implying that more Ag atoms have been consumed by the big Ag_2Te phase. Repeated APT characterization is shown in Figure S3 (Supporting Information) with good consistency.

The as-quenched sample was cooled down from the single-phase PbTe region to inhibit the precipitation of Ag_2Te. However, precipitates with different shapes, sizes, and compositions were still formed as characterized above. Presumably, the large precipitates were formed in the early stage of quenching due to the fast diffusion of Ag at high temperatures,[49,51,58] while the small spherical Ag-rich clusters were formed in the late stage of quenching when diffusion is limited at lower temperatures. It was reported that precipitates form initially as spheroids to minimize the interface energy at small sizes.[49] As the precipitates grow and the volume increases with respect to the interfacial area, their shape becomes plate-like to reduce the strain energy within the precipitates.[49] Thermal annealing could help to further probe the evolution of microstructures and the growth mechanism of precipitates, which will be studied as follows.

After annealing at 653 K for 48 h, the Ag_2Te precipitates and Ag-rich interstitial clusters evolve at the nanoscale. **Figure 2a** shows a STEM micrograph with corresponding energy dispersive X-ray spectroscopy (EDS) maps, highlighting a big Ag_2Te precipitate in the annealed sample. The phase boundary between PbTe and Ag_2Te is atomically resolved in Figure 2b, following the same OR as observed in Figure S2 (Supporting Information) (along zone axes OR-b). The protruding of Ag_2Te into PbTe along <110> direction on the (002) plane of PbTe was captured and shown in Figure S4 (Supporting Information). The large lattice mismatch between $(002)_{PbTe}$ and $(200)Ag_2Te$ causes the strain field at the growth front (Figure S4b, Supporting Information), which might attract Ag from the matrix and support the growth of Ag_2Te. Figure 2c shows the 3D APT reconstruction with a Ag_2Te precipitate featured by a high density of Ag atoms (red dots). The lattice planes in the APT reconstruction for the (200) plane of Ag_2Te and (002) plane of PbTe are shown in Figure 2d. A

Table 2. Structural and chemical statistics of small (spherical) and big (platelet or lath-shaped) precipitates, as well as the content of Pb, Te and Ag in the PbTe matrix in as-quenched and annealed samples. N_{P_s}, N_{P_b}, and N_{DS} stand for the number density of small precipitate, large precipitate, and dislocations, respectively.

Samples	N_{P_s} (m^{-3})	N_{P_b} (m^{-3})	N_{DS} (cm^{-2})	Pb (at.%)	Te (at.%)	Ag (at.%)
As-quenched	7.5×10^{24}	1.9×10^{21}	Not observed	48.61 ± 0.29	50.70 ± 0.29	0.69 ± 0.11
annealed	2.5×10^{19}	9.2×10^{18}	3.5×10^{11}	49.92 ± 0.36	49.74 ± 0.36	0.34 ± 0.05

composition profile is provided in Figure 2e obtained by the proximity histogram analyses.[59] The precipitate composition in the annealed sample is stoichiometric Ag_2Te without any observable Pb solute atoms, which is different from the results of the as-quenched sample. This means that Pb atoms were repelled out and Ag atoms were consumed from the matrix after long-term annealing. This has also been confirmed by the reduced average content of Ag in the matrix, as shown in **Table 2**. Compared with the as-quenched sample, we find fewer small spherical defects in the annealed one. The larger precipitates are more energetically favored, and they grow from dissolved small particles through the Ostwald ripening mechanism.[60] For the big lath-shaped Ag_2Te precipitate in Figure 2a, the long axis is ≈500 nm and along $[001]_{Ag_2Te}$, corresponding to the direction with smallest lattice mismatch, OR-c (see Table 1). The zone axes direction with OR-b has the second smallest lattice mismatch, and spans across the thickness dimension, ≈100 nm long. The dimension corresponding to OR-a is the shortest, ≈50 nm, corresponding to the biggest lattice mismatch. While small Ag-rich clusters with the same structure as the PbTe matrix are spherical to minimize the interface energy, bigger Ag_2Te precipitates show the OR-a/b/c with smaller dimensions along ORs with larger lattice mismatch to minimize the strain energy.

Besides the coarsening of precipitates, we have observed also high numbers of dislocations in the annealed sample. **Figure 3a** illustrates the 3D dislocation networks as delineated by 2.5 at.% Ag iso-composition surfaces. Similar curved and straight dislocations were also observed by STEM as shown in Figure 3b,c. Owing to the thermal vibration of atoms, it is inevitable to generate vacancies in solids especially when kept at high temperatures. These vacancies can be partly frozen in the material as non-equilibrium defects by a fast quenching process. APT

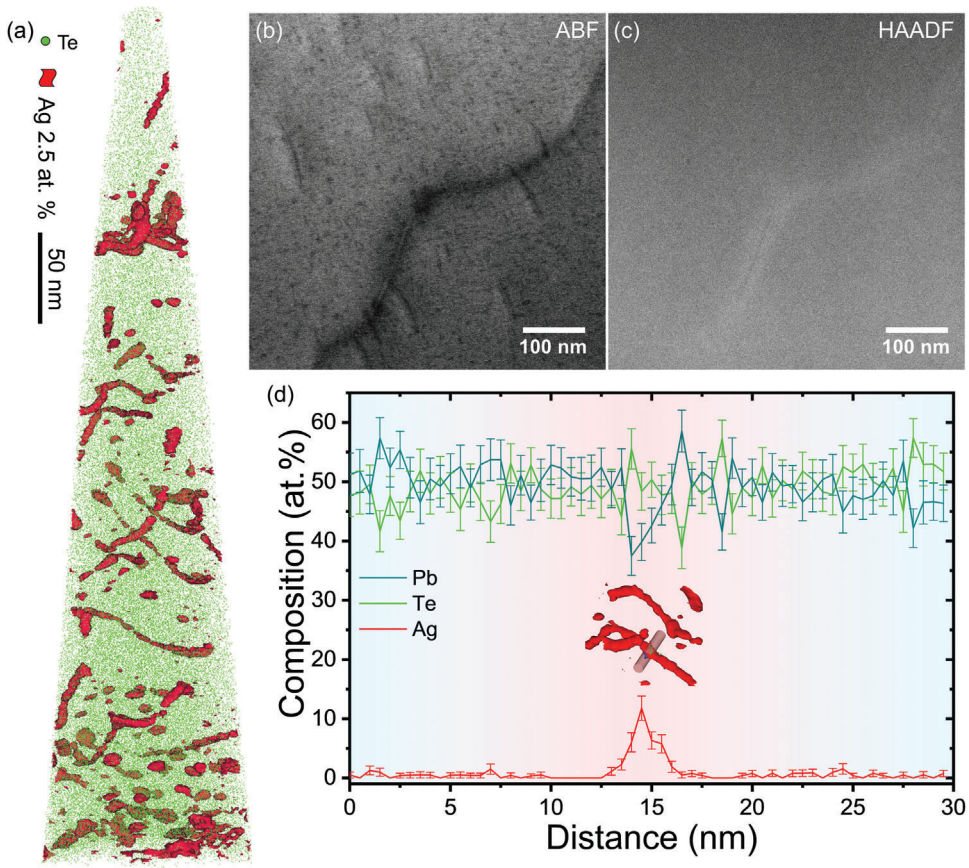

Figure 3. Dislocations in the annealed sample. a) APT reconstruction displaying the dislocation networks in 3D space; dislocations are delineated by 2.5 at.% Ag iso-composition surface. b) STEM-ABF image showing straight and curved dislocations. c) The corresponding STEM-HAADF image. d) Composition profile along the cylindrical region of interest across the dislocation line.

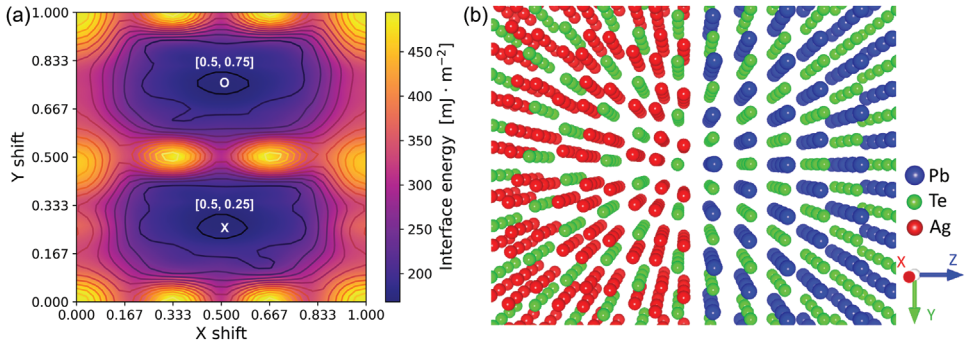

Figure 4. a) Contour maps depicting the interface energy of 72 heterostructures for the PbTe/Ag_2Te interface with varied shifts along X (OR-b: $[1\bar{1}0]_{PbTe} \parallel [010]_{Ag_2Te}$) and Y (OR-c: $[110]_{PbTe} \parallel [001]_{Ag_2Te}$) directions. The two local minima are marked with "×" [0.5, 0.25] and "○" [0.5, 0.75]. The units of X- and Y- shifts correspond to the length of the structural lattice. b) Relaxed structure of PbTe/Ag_2Te interface with lowest interface energy obtained through first-principles calculations, viewed along X-direction (OR-b: $[1\bar{1}0]_{PbTe} \parallel [010]_{Ag_2Te}$).

compositions also imply a large fraction of Pb vacancies in the as-quenched sample matrix given the high number of supersaturated Pb in Ag_2Te precipitates (Figure 1). Upon thermal annealing, these vacancies aggregate along certain planes, preferentially on the close-packed planes due to their low surface energy, forming a slice of vacancies. Finally, the vacancy layer collapses at an adequately large size, creating closed loops of edge dislocations. These supersaturated vacancies further facilitate dislocation climb and motion to increase the dislocation density. This is the so-called Bardeen-Herring source for dislocation nucleation and multiplication.[9] These dislocations create electrostatic attractions as well as chemical and elastic interactions with the Ag dopants, forming Ag-rich Cottrell atmospheres as quantified in Figure 3d. A similar Ag enrichment at dislocation cores has also been observed in our previous work.[20,21,61] Repeated APT characterizations (Figure S5, Supporting Information) were carried out to determine the average dislocation density to be 3.5×10^{11} cm^{-2}. The increased dislocation density with annealing was also found in $Na_{0.03}Eu_{0.03}Sn_{0.02}Pb_{0.92}Te$ alloy,[13] and later was associated with Na Cottrell atmospheres in $Na_{0.025}Eu_{0.03}Pb_{0.945}Te$[44] and $Na_{0.01}Pb_{0.99}Te$[62] alloys.

Although structures and orientations of the phase boundary between the PbTe matrix and Ag_2Te precipitate have been characterized (refer to Figure 2b), the question of whether this observed boundary possesses the lowest energy and detailed stacking information at the boundary region remains unclear. To further investigate the stability and geometry of the boundary, we constructed the PbTe/Ag_2Te interface models following the observed orientations of the two phases, as depicted in Figure S6 (Supporting Information). Subsequently, we carried out first-principles calculations for interface structure optimization and computed the interface free energy.

Drawing inspiration from the concept of the generalized stacking fault energy (γ–surface), which offers a comprehensive description of stacking faults and is crucial for analyzing the dislocation core and deformation mechanisms,[63] we adopted a similar approach to screen the lowest–energy interface configuration. Considering the similarity of the obtained γ–surfaces of basal stacking faults for two-phase structures, a series of heterostructures were constructed by shifting either $(002)_{PbTe}$ or $(200)_{Ag_2Te}$ slabs along X (OR-b: $[1\bar{1}0]_{PbTe} \parallel [010]_{Ag_2Te}$) and Y (OR-c: $[110]_{PbTe} \parallel [001]_{Ag_2Te}$) directions. To achieve a fine scanning mesh grid of the interface energy, fractional displacements of 1/12 and 1/6 were applied along the X- and Y- directions, respectively. A total of 72 heterostructures were involved, and the corresponding configurations at the two-phase interface are displayed in Figure S7 (Supporting Information). Contour maps of the computational interface energy of the PbTe/Ag_2Te interface with varied shifts are shown in **Figure 4a**, while the actual values are shown in the colormap in Figure S8 (Supporting Information). Due to the centro-symmetry of these heterostructures, their corresponding interface energies also exhibit centro-symmetric patterns. The PbTe/Ag_2Te interface attains stabilization for the shift vectors of [0.5, 0.25] and [0.5, 0.75], with interface energies of 168 and 169 mJ/m^2, respectively. Since the configurations of the two energy minima are structurally identical, only the structure with the shift vector [0.5, 0.25] is shown in Figure 4b. To access the stacking and structural details of these heterostructures, the side views and top views of the structures with shift vectors of [0.0, 0.0], [0.5, 0.25], and [0.5, 0.75] are displayed in Figure S9 (Supporting Information). The interfaces with the lowest interface energies calculated possess the same OR as characterized using electron microscopy (see Figure 2b). Notably, the interface structure with a shift vector of [0.0, 0.0] reveals coherent ordering of Ag_2Te layers on the $(002)_{PbTe}$ surface, accompanied by layer distortion and a significant increase in interface energy. Thus, the interface with substantial distortion is thermodynamically unfavorable.

2.2. Correlations Between Thermoelectric Properties and Microstructures

Thermoelectric transport properties of the as-quenched and annealed samples were also studied at the temperature range from 300 to 575 K, as listed in Table S1 (Supporting Information). These transport properties are measured below the annealing temperature to avoid microstructure evolution during measurement; therefore, can be better correlated with the microstructures observed. **Figure 5a,b** shows improvements in the electrical conductivity and the absolute value of Seebeck coefficients by thermal annealing. For degenerate semiconductors

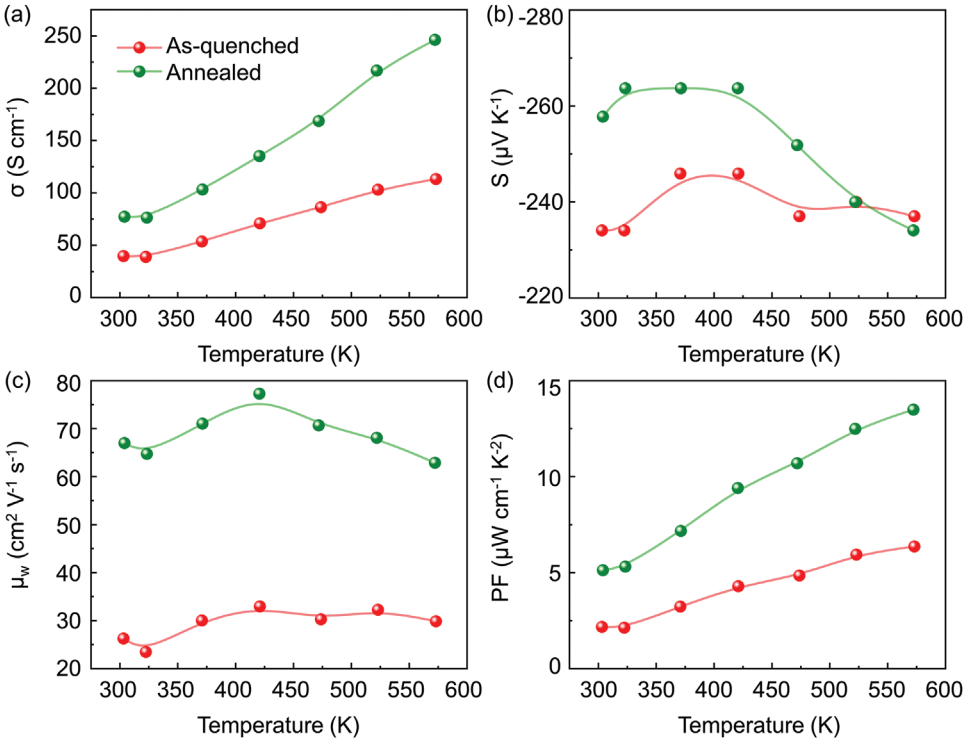

Figure 5. Temperature-dependent electrical transport properties of the as-quenched and annealed samples: a) Electrical conductivity, b) Seebeck coefficient, c) weighted mobility, d) power factor (PF).

approximated by parabolic bands and energy-independent scattering relaxation time, the Seebeck coefficient is given by[64]

$$S = \frac{8\pi^2 k_B^2}{3eh^2} m^* T\left(\frac{\pi}{3n}\right)^{2/3} \quad (1)$$

where m^* is the density-of-state effective mass, n is the carrier concentration, k_B is the Boltzmann constant, and h is the Planck constant. The increased Seebeck coefficient upon annealing indicates a decrease in carrier concentration since the electronic band structures would not change upon the coarsening of precipitates. Structural characterizations show that most of the small Ag-rich GP zones have been consumed by big Ag_2Te precipitates during the thermal annealing process via Ostwald ripening. The concentration of Ag in the PbTe matrix decreases from 0.69 at.% in the as-quenched sample to 0.34 at.% in the annealed sample, while the content of Pb changes oppositely. The coarsening of Ag_2Te precipitates occurs at the expense of Ag-rich GP zones and Ag from the matrix through the Ostwald ripening mechanism. As a result, the carrier concentration decreases with annealing, leading to enhanced Seebeck coefficients.

Owing to the complex interplay between defects, electrons and phonons, the overall effect of the microstructure on the TE properties can be evaluated by the ratio of μ_w/κ_{lat}, where μ_w is the mobility weighted by m^* and drift mobility, which is a good indicator of the power factor (PF) independent of doping level.[65] μ_w can be calculated using the experimentally determined electrical conductivity (σ) and Seebeck coefficient (S) in a simple analytic form proposed by Snyder et al.,[65] Eq. (2), where m_e is the electron mass.

$$\mu_w = \frac{3h^3\sigma}{8\pi e(2m_e k_B T)^{3/2}}\left[\frac{\exp\left[\frac{|S|}{k_B/e} - 2\right]}{1+\exp\left[-5\left(\frac{|S|}{k_B/e} - 1\right)\right]} + \frac{\frac{3}{\pi^2}\frac{|S|}{k_B/e}}{1+\exp\left[5\left(\frac{|S|}{k_B/e} - 1\right)\right]}\right] \quad (2)$$

Figure 5c shows a considerable enhancement of μ_w upon thermal annealing treatment. This can be attributed to four factors based upon the structural characterizations: i) the lowered number density of Ag_2Te precipitates; ii) the decreased concentration of Ag in the matrix; iii) the increased concentration of Pb and thus reduced content of Pb vacancy in the matrix, i.e., lattice plainification[66,67]; and iv) the relaxed strain generated by supersaturated GP zones and platelet precipitates in the as-quenched sample upon annealing. As a consequence, the PF is enhanced upon annealing as shown in Figure 5d. Enhanced carrier mobility by manipulating microstructures and compositions is key for TE coolers as summarized by Qin et al.[68]

Even though a high number density of dislocations is found in the annealed samples, they did not cause as much decrease in the mobility of electrons as the nanoscale precipitates in the as-quenched sample. The potential energy barrier for charge carrier scattering at dislocations in PbTe has been demonstrated to be small by studying individual low-angle grain boundaries.[69,70] Now we address the scattering efficiency of nanoprecipitates and dislocations on phonons. **Figure 6a** demonstrates that κ_{tot} increases with annealing. The contribution to thermal conductivity from lattice vibrations (κ_{lat}) is obtained by subtracting the electronic thermal conductivity (κ_{ele}) from the total one, where κ_{ele}

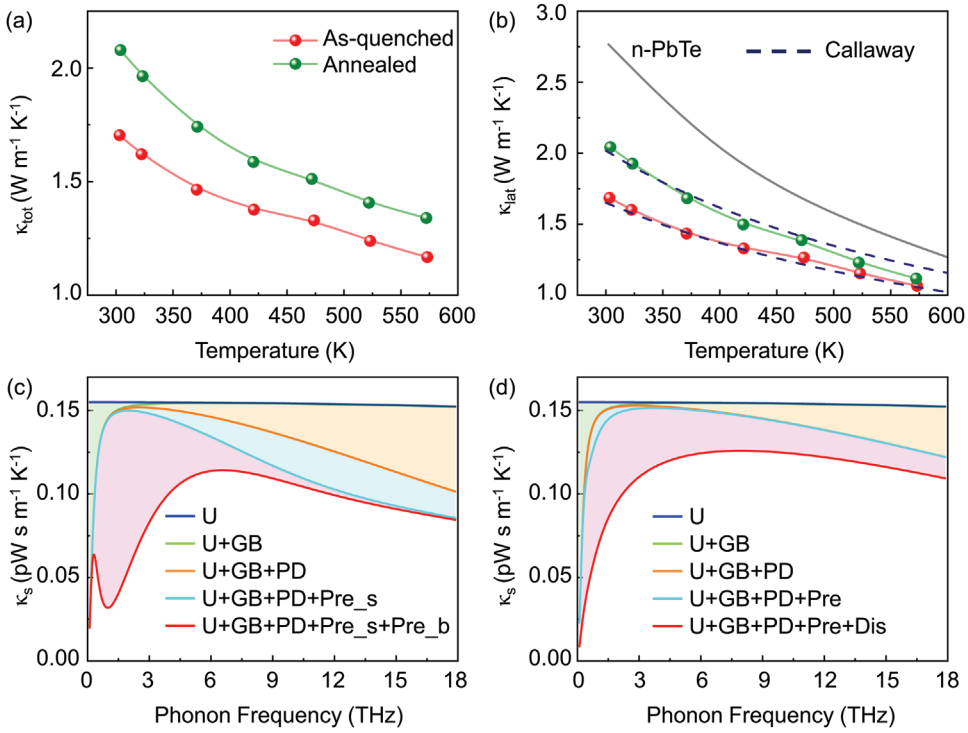

Figure 6. Temperature-dependent thermal transport properties and Debye-Callaway calculation showing the individual contribution of defects to phonon scattering. a) Total thermal conductivity, b) lattice thermal conductivity compared with that for pristine n-type PbTe taken from ref. [71]. The dashed lines depict the κ_{lat} calculated by the Debye-Callaway model for both samples using different phonon relaxation times. c) Spectral lattice thermal conductivity, κ_s, for the as-quenched sample at 300 K. The shadow areas indicate the contributions of individual structural defects to the cumulatively reduced κ_{lat}. d) κ_s for the annealed sample, where different phonon scattering sources can be observed.

can be calculated according to the Wiedemann-Franz law: $\kappa_{ele} = L\sigma T$. Here, L is the Lorenz number calculated using the single parabolic band model.[19] The lattice thermal conductivity of the annealed sample is also larger than that of the as-quenched sample but significantly lower than the reference pristine n-type PbTe (Figure 6b) without observable precipitates and dislocations.[71] To understand the individual contribution of different defects to the reduction of κ_{lat}, the Debye-Callaway model is invoked[72]:

$$\boldsymbol{\kappa}_{lat} = \frac{k_B}{2\pi^2 \upsilon}\left(\frac{k_B T}{\hbar}\right)^3 \int_0^{\Theta_D/T} \tau_{tot}(x)\frac{x^4 e^x}{(e^x-1)^2}dx \quad (3)$$

where υ is the average phonon velocity, $\hbar$ is the reduced Planck's constant, Θ_D is the Debye temperature, $x \equiv \hbar\omega/k_B T$, where ω is the phonon angular frequency. The total relaxation time, τ_{tot}, can be calculated according to Matthiessen's rule including the scattering terms from the Umklapp process (τ_U^{-1}), Grain boundaries (τ_{GB}^{-1}), point defects (τ_{PD}^{-1}), precipitates (τ_{Pre}^{-1}), as well as dislocation cores and strain fields (τ_{Dis}^{-1}).

$$\tau_{tot}^{-1} = \tau_U^{-1} + \tau_{GB}^{-1} + \tau_{PD}^{-1} + \tau_{Pre}^{-1} + \tau_{Dis}^{-1} \quad (4)$$

Detailed expressions for individual scattering mechanisms along with corresponding parameters can be found in the supplementary information. The Debye-Callaway model shows good consistency with our experimental data but with different phonon scattering sources for samples subjected to distinct annealing histories (Figure 6b). The reduced κ_{lat} in the as-quenched sample mainly stems from the extremely high number density of small spherical nanoparticles and plate-like precipitates (Table 2), leading to more than half of the reduction, while point defects also play non-negligible roles in scattering high-frequency phonons, as illustrated in the spectral lattice thermal conductivity in Figure 6c. The relative reduction in κ_{lat} by small Ag-rich clusters and big Ag_2Te lamellae is marginal in the annealed sample, as demonstrated in Figure 6d, due to their significantly decreased number density through the Ostwald ripening mechanism.[60] However, the relative contribution from Ag-decorated dislocations to the reduced κ_{lat} becomes dominant due to the enhanced strain field phonon scattering by Cottrell atmospheres,[20,44,73] even though the dislocation density is not as high as that observed in other TE alloys, which is typically on the order of 10^{12} cm^{-2}.[9–13,43]

The reason for the strong interface phonon scattering in the as-quenched sample is twofold. DFT calculations suggest that the effective mean free path of phonons in PbTe is about several tens of nanometers,[74] which is comparable to the distance between neighboring nanoprecipitates. Thus, the high-density small Ag-rich GP zones and plate-like Ag_2Te in the as-quenched sample are more effective in scattering phonons than the big precipitates in the annealed sample. The second factor is the different chemical bonding mechanisms between the PbTe matrix and Ag_2Te precipitates. **Figure** 7a,b shows the 3D distribution of Ag atoms determined by APT and the corresponding

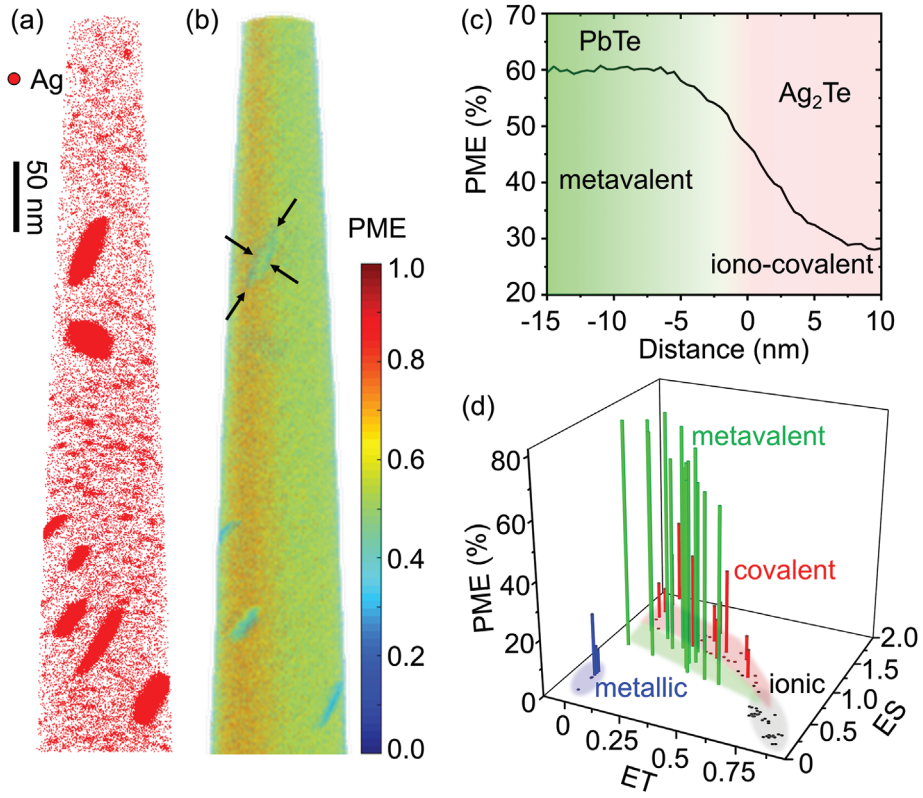

Figure 7. Chemical bonding mechanisms for the PbTe matrix and Ag_2Te precipitates revealed by laser-assisted APT. a) 3D distribution of Ag atoms showing the spherical Guinier-Preston (GP) zones and platelet precipitates. b) Corresponding 3D probability of multiple events (PME) map generated by a home-coded software. The four black arrows indicate the Ag_2Te precipitate used for PME proximity histogram calculations. c) PME profile across the interface from the PbTe matrix to the Ag_2Te precipitate. d) A collection of PME values for compounds employing different chemical bonding mechanisms plotted based on a plane coordinated by the numbers of electrons transferred (ET) and electrons shared (ES) between neighboring atoms. Data were collected from Refs. [75,77] with permission.

"probability of multiple events" (PME) map, respectively. The PME value describes the probability of dislodging more than one fragment during one successful laser pulse in APT measurements.[75] We have calculated the PME proximity histogram from the PbTe matrix to the inner core of the Ag_2Te precipitate indicated by black arrows using a method similar to the composition proximity histogram by defining an iso-concentration surface,[59] as shown in Figure 7c. The PbTe matrix exhibits a PME value of 60%, while the PME quickly drops to ≈30% in the Ag_2Te precipitate. Extensive studies have demonstrated that a high PME value (≥60%) is a hallmark of compounds utilizing metavalent bonding (MVB).[2,76,77] MVB describes a situation where adjacent atoms share half an electron pair (one electron) to form a σ-bond, unlike ordinary covalent bonding, where adjacent atoms are held together by an electron pair.[78,79] MVB compounds are characterized by a unique property portfolio,[80,81] unconventional bond rupture in laser-assisted APT,[77] as well as a peculiar electronic configuration.[78,82] Figure 7d illustrates a 3D map utilizing two variables called electrons transferred (ET) and electrons shared (ES) between neighboring atoms as the basal plane and PME as the third axis. The ET-ES map calculated by quantum chemical tools has been demonstrated to be able to separate different chemical bonding mechanisms, where MVB is prevalent in a region with small ET values and an ES close to one.[83] Figure 7d shows a strong correlation between high PME values and the MVB mechanism. Thus, we can conclude that the PbTe matrix employs MVB while the Ag_2Te precipitate utilizes iono-covalent bonding.[34,84] Since the force constant, which impacts the phonon dispersion, is closely linked to the chemical bonding mechanism, the phonon dispersions are mismatched at the phase boundary, leading to significant phonon scattering at the interface.[85]

Realizing zT enhancement requires sophisticated manipulations of the carrier concentration and microstructures.[86] The complex role of structural defects on the final zT value can be evaluated by the materials quality factor, which describes the tradeoff between electron and phonon transport, independent of the optimization of charge carrier concentrations. The quality factor, B, is determined by the ratio of μ_w/κ_{lat}, as follows[65]

$$B = \left(\frac{k_B}{e}\right)^2 \frac{8\pi e\left(2m_e k_B T\right)^{3/2} T}{3h^3} \frac{\mu_w}{\kappa_{lat}} \quad (5)$$

Figure 8a shows an increased B factor upon annealing as a result of the greatly increased weighted mobility even though the lattice thermal conductivity is higher than that of the as-quenched sample. This also demonstrates that not all

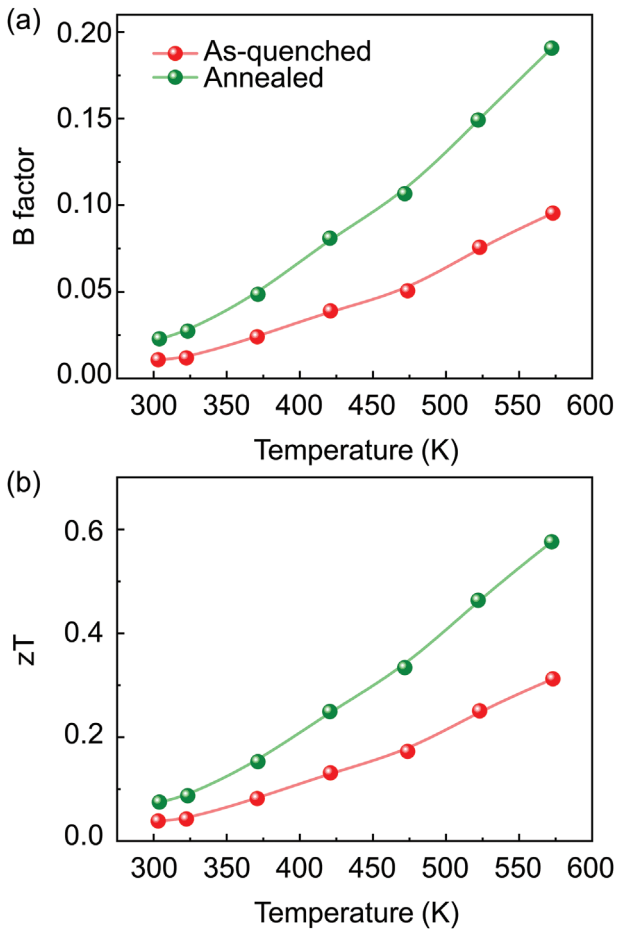

Figure 8. Temperature-dependent a) quality factor, B factor, and b) figure-of-merit, zT, for the as-quenched and annealed samples.

structural defects are beneficial to TE properties due to the complex tradeoff between electron and phonon transport for thermoelectrics. Compared to nanoprecipitates, dislocations seem to be more favorable for n-type PbTe because they can give rise to a larger B factor. Consequently, the zT value is improved in the entire measurement temperature range for the annealed sample, see Figure 8b. The zT value of 0.6 at 575 K is comparable to other PbTe-Ag_2Te alloys reported[54,55] and a higher zT can be expected at higher temperatures with optimized carrier concentration by introducing dopants such as I,[87] Bi,[21] and Sb.[71] Recent work shows that Ag_2Te precipitates and Ag-rich dislocations can provide dynamic dopants over a broad temperature range.[20,21] Thus, the optimization of carrier concentration should include both the static and dynamic doping effects. Moreover, the crystallographic orientation relationship between PbTe and Ag_2Te can be utilized to tailor the transport properties by growing PbTe single crystals embedded with well-aligned Ag_2Te precipitates.

3. Conclusion

Structural evolution of $(PbTe)_{0.97}(Ag_2Te)_{0.03}$ alloys was investigated by quenching and annealing, revealing the relationships between microstructure, composition, chemical bonding, and TE properties. A high number density of small spheroidal Ag-rich clusters and plate-like Ag_2Te precipitates were observed in the as-quenched sample. Explicit crystallographic orientation relationships between PbTe and Ag_2Te were determined for the specimens that underwent different nucleation and growth processes of precipitates. It is found that the growth of Ag_2Te phase is confined within the interface of $(002)_{PbTe}$ and $(200)_{Ag_2Te}$, forming a plate-like shape. The coarsening of Ag_2Te precipitates by annealing was accomplished by consuming small Ag-rich clusters through the Ostwald ripening mechanism. As a result, the carrier concentration is decreased and the weighted mobility is greatly increased due to the coarsened precipitates and strain relaxation. Debye-Callaway calculations demonstrate that small Ag-rich clusters and platelet precipitates are the main phonon scattering source in the as-quenched sample, while dislocation phonon scattering becomes more prominent in the annealed sample. Due to the tradeoff between weighted mobility and lattice thermal conductivity, the annealed sample with dislocation-dominated microstructures shows a higher B factor and zT value. This work provides a thorough investigation of the structural evolution of Ag_2Te precipitates in PbTe and its impact on TE properties, shedding light on microstructural design for thermoelectrics.

4. Experimental Section

Sample Preparation: Materials were synthesized from raw Pb powder (99.96%, Riedel-de Haen), Te broken ingots (99.99%, Strem Chemicals), and Ag granules (99.999%, Alfa Aesar) by weighing according to the nominal composition of $(PbTe)_{0.97}(Ag_2Te)_{0.03}$ and sealing in quartz tubes under dynamic vacuum. The sealed tubes were heated to 1273 K in 12 h and dwelled for 6 h in a vertical programmable tube furnace to ensure a homogeneous melting of the mixture, followed by moderate cooling down to 973 K and dwelled for 48 h to enable homogenization. Subsequently, the melts were rapidly cooled down by quenching in iced water. The solidified ingots were then hand-ground into fine powders with agate mortar and pestle in an Ar-filled glove box. The resulting powders were consolidated by hot pressing at 923 K in the single-phase region for 30 min under uniaxial pressure of 45 MPa for 15 min under flowing Ar-7% H_2 gas mixture, followed by iced water quenching. This is defined as the "as-quenched" sample throughout the manuscript. To study the microstructure evolution, the hot-pressed pellet was annealed at 653 K in a two-phase region for 48 h in a sealed quartz ampoule under a 120 torr Ar-7% H_2 atmosphere followed by ice-water quenching. This is defined as the "annealed" sample. Powder X-ray diffraction (XRD) was performed for phase identification applying a Rigaku *Smartlab* diffractometer operating with Cu-K_α radiation, angular resolution of 0.02°, and angular range of 20 – 90°. The XRD patterns appear in Figure S10 (Supporting Information); both correspond to the rock-salt PbTe ($Fm\bar{3}m$) structure, which was fully indexed. The presence of nanometer-size Ag_2Te precipitates could not be identified by XRD. The pattern corresponding to rock-salt PbTe structure was preserved for different changes in microstructure and processing conditions such as the introduction of impurities and second phases, hand-grinding, or ball milling of the powders.

Scanning Transmission Electron Microscopy (STEM): STEM lamellae were prepared using a dual beam SEM-FIB (*Helios NanoLab* 650) and cleaned at 5 kV to eliminate the Ga-ion contamination and surface amorphization. STEM investigations were carried out using an aberration-corrected *Titan Themis* microscope operated at 300 kV. The convergence angle of the probe was 24 mrad, and the collection angles of the ABF and HAADF detectors were 8–16 and 73–352 mrad, respectively. Image analyses were done using the *ImageJ* and *DigitalMicrograph* software. EDS spectrum imaging was acquired using a *SuperX* detector. Multivariate statistical

analysis was applied to reduce the noise and facilitate quantitative analysis of the hyperspectral datasets.[88]

Atom Probe Tomography (APT): Needle-shaped APT specimens were prepared following the standard "lift-out" method.[89] APT measurements were conducted using a local electron atom probe (LEAP 4000X Si, Cameca) by applying 10-ps, 25-pJ ultraviolet (wavelength = 355 nm) laser pulses with a detection rate of 1 ion per 100 pulses on average (1.0%), a pulse repetition rate of 200 kHz, a base temperature of 40 K, and an ion flight path of 160 mm. APT data were processed using Cameca's integrated visualization and analysis software IVAS 3.8.0.

Thermoelectric Properties Measurement: All the TE transport properties were measured perpendicular to the pressing direction to minimize measurement errors. Seebeck coefficient and electrical conductivity were measured simultaneously for bar-shaped specimens with dimensions of $12 \times 3 \times 3$ mm^3 by the Netzsch SBA-458 *Nemesis* system under an Ar atmosphere. The total thermal conductivity was obtained according to $\kappa_{tot} = DC_p\rho$. The thermal diffusivity, D, was measured for a disk-shaped specimen with a diameter of 6 or 8 mm and a thickness of 1.5 mm using the laser flash analysis method using the Netzsch LFA-457 *Microflash* apparatus. Heat capacity, C_p, (in k_B per atom units) was evaluated by $3.07 + 4.7 \times 10^{-4} \times$ (T-300) with an uncertainty of only 2% for all the lead chalcogenides at T > 300 K.[55] Mass density, ρ, was calculated based on the geometric dimensions and mass. Note that all samples have a density higher than 98% of the theoretical values, indicating that density has negligible impacts on thermal transport. Since this work focuses on the Ostwald ripening upon annealing and the fundamental relationship between microstructures and properties, the measurement temperature was set below 600 K to comply with the annealing temperature. Thus, the TE properties could be better correlated with the stable microstructures, avoiding significant microstructure evolution during measurements.

Computational Methods: The interface energies of sampled PbTe/Ag_2Te interfaces at 0 K were determined through first-principles calculations based on total energy calculations utilizing DFT. All the calculations were performed using the Vienna *ab-initio* Simulation Package VASP.[90] The electron–ion interactions were represented within the projector augmented wave (PAW) method,[91] and the exchange–correlation part of the Kohn–Sham potential employed the generalized gradient approximation parameterized by Perdew, Burke, and Ernzerhof. A plane-wave energy cutoff of 500 eV was applied, and Γ–centered Monkhorst–Pack k–points meshes of $6 \times 6 \times 6$ and $4 \times 6 \times 4$ were used for the conventional cells of PbTe (space group: $Fm\bar{3}m$) and Ag_2Te (space group: $P2_1/c$), respectively. As demonstrated in the experimental section, the growth of the Ag_2Te phase was confined within the interface comprising the $(002)_{PbTe}$ and $(200)_{Ag_2Te}$ planes. Accordingly, the PbTe/Ag_2Te interface slab was modeled as a heterostructure between 1×2 $(002)_{PbTe}$ and 1×1 $(200)_{Ag_2Te}$ slabs, as illustrated in Figure 4. A vacuum layer of ~16 Å along the Z direction was introduced to eliminate interactions between neighboring layers. The lattice parameters of the interface slab model were 4.638 Å × 9.277 Å × 54.254 Å, encompassing the vacuum. During optimization, all atoms were allowed to relax, with a few bottom layers of atoms on both sides fixed. The fixed layers were visually highlighted within an orange box, as depicted in Figure S1. A Γ–centered *k*-point mesh of $4 \times 2 \times 1$ was set for the geometrical optimization of these slab models. Gaussian smearing with a width of 0.05 eV and fully automatic optimization of projection operators were chosen. All structures underwent optimization using the Blocked–Davidson algorithm until the energy converged to less than 10^{-6} eV, and the Hellmann–Feynman forces converged to less than 10^{-3} eV/Å.

The interface energy γ was determined by subtracting the total energy of the interface slab model from the total energies of the corresponding bulk phases. As the vacuum along the Z direction was included in the created interface models, the $(002)_{PbTe}$ and $(200)_{Ag_2Te}$ surfaces were generated, and their surface energies need to be further subtracted. This could be expressed as:[92]

$$\gamma = \frac{1}{A}\left(E^{int}_{PbTe/Ag_2Te} - N_{PbTe}E^{bulk}_{PbTe} - N_{Ag_2Te}E^{bulk}_{Ag_2Te}\right) - \gamma^{(002)}_{PbTe} - \gamma^{(200)}_{Ag_2Te} \quad (6)$$

Here, E^{int}_{PbTe/Ag_2Te}, E^{bulk}_{PbTe} and $E^{bulk}_{Ag_2Te}$ represent the total energy of interface structures, bulk PbTe and bulk Ag_2Te, respectively. N_{PbTe} and N_{Ag_2Te} are the numbers of bulk PbTe and Ag_2Te unit cells composing the interface structures, respectively. $\gamma^{(002)}_{PbTe}$ and $\gamma^{(200)}_{Ag_2Te}$ denote the surface energy of $(002)_{PbTe}$ and $(200)_{Ag_2Te}$ surfaces. *A* is the interface area.

The surface energies ($\gamma^{(002)}_{PbTe}$ and $\gamma^{(200)}_{Ag_2Te}$) are defined as the difference between the free energy of surface atoms and that of atoms in the bulk. In these cases, the surfaces flanking the interface models were frozen during structural optimization, and as such, the structure of the slabs was not relaxed. The formulation is as follows:[93]

$$\gamma_i = \frac{1}{2A_i}\left(E^{slab}_i(N_i) - N_iE^{bulk}_i\right), \ (i = (002)_{PbTe} \text{ or } (200)_{Ag_2Te}) \quad (7)$$

where $E^{slab}_i(N_i)$ is the total energy of a N_i-layer slab calculated with a sufficiently large value of N_i, E^{bulk}_i denotes the bulk energy, and A_i represents the corresponding surface area.

Supporting Information

Supporting Information is available from the Wiley Online Library or from the author.

Acknowledgements

S.Z. and C.S. acknowledge Deutsche Forschungsgemeinschaft (DFG) within the Collaborative Research Center SFB 1394 "Structural and Chemical Atomic Complexity—From Defect Phase Diagrams to Materials Properties" (Project ID 409476157, project group B01). Y.A. acknowledges the Grand Technion Energy Program (GTEP) and the Jordan and Irene Tark Aerospace Research Fund. The authors thank Prof. Dierk Raabe and Prof. Baptiste Gault from MPIE for proofreading the manuscript and helpful discussions.

Open access funding enabled and organized by Projekt DEAL.

Conflict of Interest

The authors declare no conflict of interest.

Data Availability Statement

The data that support the findings of this study are available from the corresponding author upon reasonable request.

Keywords

dislocation, lead telluride, metavalent bonding, Ostwald ripening, thermoelectric

Received: December 22, 2023
Revised: February 1, 2024
Published online: February 21, 2024

[1] J. He, T. M. Tritt, *Science* **2017**, *357*, eaak9997.
[2] Y. Yu, M. Cagnoni, O. Cojocaru-Mirédin, M. Wuttig, *Adv. Funct. Mater.* **2020**, *30*, 1904862.

[3] Y. Yu, C. Zhou, S. Zhang, M. Zhu, M. Wuttig, C. Scheu, D. Raabe, G. J. Snyder, B. Gault, *Mater. Today* **2020**, *32*, 260.
[4] G. Tan, L. D. Zhao, M. G. Kanatzidis, *Chem. Rev.* **2016**, *116*, 12123.
[5] T. Zhu, Y. Liu, C. Fu, J. P. Heremans, G. J. Snyder, X. Zhao, *Adv. Mater.* **2017**, *29*, 1605884.
[6] X. Tang, Z. Li, W. Liu, Q. Zhang, C. Uher, *Interdiscip. Mater.* **2022**, *1*, 88.
[7] Q. Yan, M. G. Kanatzidis, *Nat. Mater.* **2022**, *21*, 503.
[8] N. A. Heinz, T. Ikeda, Y. Pei, G. J. Snyder, *Adv. Funct. Mater.* **2014**, *24*, 2135.
[9] Z. Chen, B. Ge, W. Li, S. Lin, J. Shen, Y. Chang, R. Hanus, G. J. Snyder, Y. Pei, *Nat. Commun.* **2017**, *8*, 13828.
[10] C. Zhou, Y. K. Lee, J. Cha, B. Yoo, S. P. Cho, T. Hyeon, I. Chung, *J. Am. Chem. Soc.* **2018**, *140*, 9282.
[11] Y. Xiao, Y. Wu, P. Nan, H. Dong, Z. Chen, Z. Chen, H. Gu, B. Ge, W. Li, Y. Pei, *Chem* **2020**, *6*, 523.
[12] Z. Chen, Z. Jian, W. Li, Y. Chang, B. Ge, R. Hanus, J. Yang, Y. Chen, M. Huang, G. J. Snyder, Y. Pei, *Adv. Mater.* **2017**, *29*, 1606768.
[13] Y. Wu, Z. Chen, P. Nan, F. Xiong, S. Lin, X. Zhang, Y. Chen, L. Chen, B. Ge, Y. Pei, *Joule* **2019**, *3*, 1276.
[14] C. Zhang, Q. Lai, W. Wang, X. Zhou, K. Lan, L. Hu, B. Cai, M. Wuttig, J. He, F. Liu, Y. Yu, *Adv. Sci.* **2023**, *10*, 2302688.
[15] Z. Liu, T. Hong, L. Xu, S. Wang, X. Gao, C. Chang, X. Ding, Y. Xiao, L. D. Zhao, *Interdiscip. Mater.* **2022**, *2*, 161.
[16] S. Liu, Y. Yu, D. Wu, X. Xu, X. Chao, Z. Yang, J. He, *Small* **2021**, *17*, 2104496.
[17] H. Lee, T. Kim, S. C. Son, J. Kim, D. Kim, J. Lee, I. Chung, *Mater. Today Phy.* **2023**, *31*, 100986.
[18] L. Fu, M. Yin, D. Wu, W. Li, D. Feng, L. Huang, J. He, *Energy Environ. Sci.* **2017**, *10*, 2030.
[19] Y. Pei, Z. M. Gibbs, A. Gloskovskii, B. Balke, W. G. Zeier, G. J. Snyder, *Adv. Energy Mater.* **2014**, *4*, 1400486.
[20] Z.-Y. Huang, F. Wang, C. Jung, S. Zhang, F. Zu, C. Zhou, Y. Yu, *Mater. Today Phys.* **2023**, *37*, 101198.
[21] Y. Yu, C. Zhou, X. Zhang, L. Abdellaoui, C. Doberstein, B. Berkels, B. Ge, G. Qiao, C. Scheu, M. Wuttig, O. Cojocaru-Mirédin, S. Zhang, *Nano Energy* **2022**, *101*, 107576.
[22] Z.-Y. Huang, H. Zhang, L. Yang, B. Zhu, K. Zheng, M. Hong, Y. Yu, F.-Q. Zu, J. Zou, Z.-G. Chen, *Mater. Today Energy* **2018**, *9*, 383.
[23] C. Zhang, G. Yan, Y. Wang, X. Wu, L. Hu, F. Liu, W. Ao, O. Cojocaru-Mirédin, M. Wuttig, G. J. Snyder, Y. Yu, *Adv. Energy Mater.* **2023**, *13*, 2203361.
[24] C. Zhou, Y. Yu, Y. K. Lee, O. Cojocaru-Mirédin, B. Yoo, S.-P. Cho, J. Im, M. Wuttig, T. Hyeon, I. Chung, *J. Am. Chem. Soc.* **2018**, *140*, 15535.
[25] M. S. Dresselhaus, G. Chen, M. Y. Tang, R. G. Yang, H. Lee, D. Z. Wang, Z. F. Ren, J. P. Fleurial, P. Gogna, *Adv. Mater.* **2007**, *19*, 1043.
[26] C. Gayner, L. T. Menezes, Y. Natanzon, Y. Kauffmann, H. Kleinke, Y. Amouyal, *ACS Appl. Mater. Interfaces* **2023**, *15*, 13012.
[27] C. Gayner, Y. Natanzon, Y. Amouyal, *ACS Appl. Mater. Interfaces* **2022**, *14*, 4035.
[28] Y. Amouyal, Y. Gelbstein, D. Fuks, *Adv. Theory Simul.* **2018**, *1*, 1800072.
[29] J. J. Kuo, Y. Yu, S. D. Kang, O. Cojocaru-Miredin, M. Wuttig, G. J. Snyder, *Adv. Mater. Interfaces* **2019**, *6*, 1900429.
[30] H. Wang, A. D. LaLonde, Y. Pei, G. J. Snyder, *Adv. Funct. Mater.* **2013**, *23*, 1586.
[31] D. Bao, J. Chen, Y. Yu, W. Liu, L. Huang, G. Han, J. Tang, D. Zhou, L. Yang, Z.-G. Chen, *Chem. Eng. J.* **2020**, *388*, 124295.
[32] J. He, J. Androulakis, M. G. Kanatzidis, V. P. Dravid, *Nano Lett.* **2012**, *12*, 343.
[33] J. He, J. R. Sootsman, S. N. Girard, J.-C. Zheng, J. Wen, Y. Zhu, M. G. Kanatzidis, V. P. Dravid, *J. Am. Chem. Soc.* **2010**, *132*, 8669.
[34] C. Rodenkirchen, M. Cagnoni, S. Jakobs, Y. Cheng, J. Keutgen, Y. Yu, M. Wuttig, O. Cojocaru-Mirédin, *Adv. Funct. Mater.* **2020**, *30*, 1910039.
[35] D. An, J. Wang, J. Zhang, X. Zhai, Z. Kang, W. Fan, J. Yan, Y. Liu, L. Lu, C.-L. Jia, M. Wuttig, O. Cojocaru-Mirédin, S. Chen, W. Wang, G. J. Snyder, Y. Yu, *Energy Environ. Sci.* **2021**, *14*, 5469.
[36] T. Grossfeld, A. Sheskin, Y. Gelbstein, Y. Amouyal, *Crystals* **2017**, *7*, 281.
[37] A. Sheskin, T. Schwarz, Y. Yu, S. Zhang, L. Abdellaoui, B. Gault, O. Cojocaru-Miredin, C. Scheu, D. Raabe, M. Wuttig, Y. Amouyal, *ACS Appl. Mater. Interfaces* **2018**, *10*, 38994.
[38] J. Byrnes, D. R. G. Mitchell, S. Aminorroaya Yamini, *Mater. Today Phys.* **2020**, *13*, 100190.
[39] J. Zhang, D. Wu, D. He, D. Feng, M. Yin, X. Qin, J. He, *Adv. Mater.* **2017**, *29*, 1703148.
[40] Z.-Z. Luo, S. Cai, S. Hao, T. P. Bailey, Y. Luo, W. Luo, Y. Yu, C. Uher, C. Wolverton, V. P. Dravid, Z. Zou, Q. Yan, M. G. Kanatzidis, *Energy Environ. Sci.* **2022**, *15*, 368.
[41] H.-T. Liu, Q. Sun, Y. Zhong, Q. Deng, L. Gan, F.-L. Lv, X.-L. Shi, Z.-G. Chen, R. Ang, *Nano Energy* **2022**, *91*, 106706.
[42] S. Wang, Y. Xiao, Y. Chen, S. Peng, D. Wang, T. Hong, Z. Yang, Y. Sun, X. Gao, L.-D. Zhao, *Energy Environ. Sci.* **2021**, *14*, 451.
[43] L. You, Y. Liu, X. Li, P. Nan, B. Ge, Y. Jiang, P. Luo, S. Pan, Y. Pei, W. Zhang, G. J. Snyder, J. Yang, J. Zhang, J. Luo, *Energy Environ. Sci.* **2018**, *11*, 1848.
[44] L. Abdellaoui, Z. Chen, Y. Yu, T. Luo, R. Hanus, T. Schwarz, R. Bueno Villoro, O. Cojocaru-Mirédin, G. J. Snyder, D. Raabe, Y. Pei, C. Scheu, S. Zhang, *Adv. Funct. Mater.* **2021**, *31*, 2101214.
[45] C. Zhou, Y. Yu, Y. L. Lee, B. Ge, W. Lu, O. Cojocaru-Miredin, J. Im, S. P. Cho, M. Wuttig, Z. Shi, I. Chung, *J. Am. Chem. Soc.* **2020**, *142*, 15172.
[46] B. Ge, H. Lee, J. Im, Y. Choi, S.-Y. Kim, J. Y. Lee, S.-P. Cho, Y.-E. Sung, K.-Y. Choi, C. Zhou, Z. Shi, I. Chung, *Energy Environ. Sci.* **2023**, *16*, 3994.
[47] L. Xu, Y. Xiao, S. Wang, B. Cui, D. Wu, X. Ding, L. D. Zhao, *Nat. Commun.* **2022**, *13*, 6449.
[48] Y. J. Kim, L. D. Zhao, M. G. Kanatzidis, D. N. Seidman, *ACS Appl. Mater. Interfaces* **2017**, *9*, 21791.
[49] J. L. Lensch-Falk, J. D. Sugar, M. A. Hekmaty, D. L. Medlin, *J. Alloys Compd.* **2010**, *504*, 37.
[50] X. Wang, I. Veremchuk, U. Burkhardt, M. Bobnar, H. Böttner, C.-Y. Kuo, C.-T. Chen, C.-F. Chang, J.-T. Zhao, Y. Grin, *J. Mater. Chem. C* **2018**, *6*, 9482.
[51] K. Bergum, T. Ikeda, G. Jeffrey Snyder, *J. Solid State Chem.* **2011**, *184*, 2543.
[52] F. Wald, *J. Less-Common Met.* **1967**, *13*, 579.
[53] Y. Pei, N. A. Heinz, A. LaLonde, G. J. Snyder, *Energy Environ. Sci.* **2011**, *4*, 3640.
[54] Y. Pei, J. Lensch-Falk, E. S. Toberer, D. L. Medlin, G. J. Snyder, *Adv. Funct. Mater.* **2011**, *21*, 241.
[55] Y. Pei, A. F. May, G. J. Snyder, *Adv. Energy Mater.* **2011**, *1*, 291.
[56] B. Gault, A. Chiaramonti, O. Cojocaru-Mirédin, P. Stender, R. Dubosq, C. Freysoldt, S. K. Makineni, T. Li, M. Moody, J. M. Cairney, *Nat. Rev. Methods Primers* **2021**, *1*, 51.
[57] H. Duparc, O. B. M., *Metall. Mater. Trans. B* **2010**, *41*, 925.
[58] M. H. Dahan, A. Baranovskiy, Y. Natanzon, Y. Amouyal, *Acta Mater.* **2021**, *202*, 243.
[59] O. C. Hellman, J. A. Vandenbroucke, J. Rüsing, D. Isheim, D. N. Seidman, *Microsc. Microanal.* **2000**, *6*, 437.
[60] L. Ratke, P. W. Voorhees, *Growth and Coarsening: Ostwald Ripening in Material Processing*, Springer, Berlin, Germany **2013**.
[61] Y. Yu, S. Zhang, A. M. Mio, B. Gault, A. Sheskin, C. Scheu, D. Raabe, F. Zu, M. Wuttig, Y. Amouyal, *ACS Appl. Mater. Interfaces* **2018**, *10*, 3609.
[62] J. P. Male, L. Abdellaoui, Y. Yu, S. Zhang, N. Pieczulewski, O. Cojocaru-Mirédin, C. Scheu, G. J. Snyder, *Adv. Funct. Mater.* **2021**, *31*, 2108006.
[63] A. Datta, U. Ramamurty, S. Ranganathan, U. V. Waghmare, *Comput. Mater. Sci.* **2006**, *37*, 69.

[64] Z. Wang, L. Ding, L. Liu, Z. Tan, H. Pan, P. Jiang, W. Wu, Y. Yu, *Scr. Mater.* **2023**, *228*, 115315.
[65] G. J. Snyder, A. H. Snyder, M. Wood, R. Gurunathan, B. H. Snyder, C. Niu, *Adv. Mater.* **2020**, *32*, 2001537.
[66] D. Liu, D. Wang, T. Hong, Z. Wang, Y. Wang, Y. Qin, L. Su, T. Yang, X. Gao, Z. Ge, B. Qin, L.-D. Zhao, *Science* **2023**, *380*, 841.
[67] M. Zhang, Z. Gao, Q. Lou, Q. Zhu, J. Wang, Z. Han, C. Fu, T. Zhu, *Adv. Funct. Mater.* **2024**, *34*, 2307864.
[68] B. Qin, L.-D. Zhao, *Science* **2022**, *378*, 832.
[69] R. Wu, Y. Yu, S. Jia, C. Zhou, O. Cojocaru-Miredin, M. Wuttig, *Nat. Commun.* **2023**, *14*, 719.
[70] Y. Yu, M. Wuttig, *Nano Res. Energy* **2023**, *2*, e9120057.
[71] G. Tan, C. C. Stoumpos, S. Wang, T. P. Bailey, L.-D. Zhao, C. Uher, M. G. Kanatzidis, *Adv. Energy Mater.* **2017**, *7*, 1700099.
[72] Y. Yu, D.-S. He, S. Zhang, O. Cojocaru-Mirédin, T. Schwarz, A. Stoffers, X.-Y. Wang, S. Zheng, B. Zhu, C. Scheu, D. Wu, J.-Q. He, M. Wuttig, Z.-Y. Huang, F.-Q. Zu, *Nano Energy* **2017**, *37*, 203.
[73] Q. Zhang, Y. Lin, N. Lin, Y. Yu, F. Liu, C. Fu, B. Ge, O. Cojocaru-Mirédin, T. Zhu, X. Zhao, *Mater. Today Phys.* **2022**, *22*, 100573.
[74] Q. Song, T.-H. Liu, J. Zhou, Z. Ding, G. Chen, *Mater. Today Phys.* **2017**, *2*, 69.
[75] Y. Yu, O. Cojocaru-Mirédin, M. Wuttig, *Phys. Status Solidi A* **2023**, 2300425.
[76] Y. Yu, C. Zhou, T. Ghosh, C. F. Schon, Y. Zhou, S. Wahl, M. Raghuwanshi, P. Kerres, C. Bellin, A. Shukla, O. Cojocaru-Miredin, M. Wuttig, *Adv. Mater.* **2023**, *35*, 2300893.
[77] M. Zhu, O. Cojocaru-Miredin, A. M. Mio, J. Keutgen, M. Kupers, Y. Yu, J. Y. Cho, R. Dronskowski, M. Wuttig, *Adv. Mater.* **2018**, *30*, 1706735.
[78] M. Wuttig, C.-F. Schön, J. Lötfering, P. Golub, C. Gatti, J.-Y. Raty, *Adv. Mater.* **2022**, *35*, 2208485.
[79] W. Yao, Y. Zhang, T. Lyu, W. Huang, N. Huang, X. Li, C. Zhang, F. Liu, M. Wuttig, Y. Yu, M. Hong, L. Hu, *The Innovation* **2023**, *4*, 100522.
[80] M. Wuttig, V. L. Deringer, X. Gonze, C. Bichara, J. Y. Raty, *Adv. Mater.* **2018**, *30*, 1803777.
[81] R. Arora, U. V. Waghmare, C. N. R. Rao, *Adv. Mater.* **2022**, *35*, 2208724.
[82] Y. Cheng, S. Wahl, M. Wuttig, *Phys. Status Solidi Rapid Res. Lett.* **2020**, *15*, 2000482.
[83] J. Y. Raty, M. Schumacher, P. Golub, V. L. Deringer, C. Gatti, M. Wuttig, *Adv. Mater.* **2019**, *31*, 1806280.
[84] Y. Liu, X. Zhang, P. Nan, B. Zou, Q. Zhang, Y. Hou, S. Li, Y. Gong, Q. Liu, B. Ge, O. Cojocaru-Mirédin, Y. Yu, Y. Zhang, G. Chen, M. Wuttig, G. Tang, *Adv. Funct. Mater.* **2022**, *32*, 2209980.
[85] D. G. Cahill, P. V. Braun, G. Chen, D. R. Clarke, S. Fan, K. E. Goodson, P. Keblinski, W. P. King, G. D. Mahan, A. Majumdar, H. J. Maris, S. R. Phillpot, E. Pop, L. Shi, *Appl. Phys. Rev.* **2014**, *1*, 011305.
[86] Y. Xiao, L.-D. Zhao, *Science* **2020**, *367*, 1196.
[87] S. Wang, C. Chang, S. Bai, B. Qin, Y. Zhu, S. Zhan, J. Zheng, S. Tang, L. D. Zhao, *Chem. Mater.* **2023**, *35*, 755.
[88] S. Zhang, C. Scheu, *Microscopy* **2018**, *67*, i133.
[89] K. Thompson, D. Lawrence, D. J. Larson, J. D. Olson, T. F. Kelly, B. Gorman, *Ultramicroscopy* **2007**, *107*, 131.
[90] G. Kresse, J. Furthmüller, *Phys. Rev. B* **1996**, *54*, 11169.
[91] G. Kresse, D. Joubert, *Phys. Rev. B* **1999**, *59*, 1758.
[92] W. Liu, J. C. Li, W. T. Zheng, Q. Jiang, *Phys. Rev. B* **2006**, *73*, 205421.
[93] J. Li, M. Zhang, Y. Zhou, G. Chen, *Appl. Surf. Sci.* **2014**, *307*, 593.